AGU PUBLICATIONS

Journal of Advances in Modeling Earth Systems

RESEARCH ARTICLE

10.1002/2017MS000913

Key Points:
- MJO intensifies with warming, likely in association with changes in tropical rainfall variability
- The MJO exhibits faster eastward propagation with warming
- Zonal scale and depth of the MJO increase with warming

Correspondence to:
Á. F. Adames,
Angel.Adames-Corraliza@noaa.gov

Citation:
Adames, Á. F., D. Kim, A. H. Sobel, A. Del Genio, and J. Wu (2017), Changes in the structure and propagation of the MJO with increasing CO_2, *J. Adv. Model. Earth Syst.*, *9*, 1251–1268, doi:10.1002/2017MS000913.

Received 6 JAN 2017
Accepted 28 APR 2017
Accepted article online 8 MAY 2017
Published online 22 MAY 2017

Changes in the structure and propagation of the MJO with increasing CO_2

Ángel F. Adames[1], Daehyun Kim[2], Adam H. Sobel[3], Anthony Del Genio[4], and Jingbo Wu[3]

[1]Geophysical Fluid Dynamics Laboratory, Princeton, New Jersey, USA, [2]Department of Atmospheric Sciences, University of Washington, Seattle, Washington, USA, [3]Department of Applied Physics and Applied Mathematics, and Department of Earth and Environmental Sciences, and Lamont-Doherty Earth Observatory, Columbia University, New York, New York, USA, [4]NASA Goddard Institute for Space Studies, New York, New York, USA

Abstract Changes in the Madden-Julian Oscillation (MJO) with increasing CO_2 concentrations are examined using the Goddard Institute for Space Studies Global Climate Model (GCM). Four simulations performed with fixed CO_2 concentrations of 0.5, 1, 2, and 4 times preindustrial levels using the GCM coupled with a mixed layer ocean model are analyzed in terms of the basic state, rainfall, moisture and zonal wind variability, and the structure and propagation of the MJO. The GCM simulates basic state changes associated with increasing CO_2 that are consistent with results from earlier studies: column water vapor increases at $\sim$7.1% K^{-1}, precipitation also increases but at a lower rate ($\sim$3% K^{-1}), and column relative humidity shows little change. Moisture and rainfall variability intensify with warming while zonal wind variability shows little change. Total moisture and rainfall variability increases at a rate this is similar to that of the mean state change. The intensification is faster in the MJO-related anomalies than in the total anomalies, though the ratio of the MJO band variability to its westward counterpart increases at a much slower rate. On the basis of linear regression analysis and space-time spectral analysis, it is found that the MJO exhibits faster eastward propagation, faster westward energy dispersion, a larger zonal scale, and deeper vertical structure in warmer climates.

Plain Language Summary Changes in the Madden-Julian Oscillation (MJO) with increasing carbon dioxide (CO_2) concentrations are examined using the Goddard Institute for Space Studies Global Climate Model (GCM). Four simulations performed with varying amounts of CO_2 concentrations. We analyze the climatology and variability in rainfall and water vapor, and the structure and propagation of the MJO. The GCM simulates basic state changes associated with increasing CO_2 that are consistent with results from earlier studies: column water vapor increases at ~7.1 % per degree warming, while precipitation also increases but at a lower rate, and column relative humidity shows little change. Moisture and rainfall variability intensify with warming. Total moisture and rainfall variability increases at a rate that is similar to that of the mean state change, and it is faster at the intraseasonal timescale. It is also found that the MJO exhibits faster eastward propagation, a larger zonal scale and deeper vertical structure in warmer climates.

1. Introduction

The Madden-Julian Oscillation [*Madden and Julian*, 1971, 1972] is one of the most distinct and prominent modes of tropical intraseasonal (30–90 day) variability [*Zhang*, 2005; *Lau and Waliser*, 2011]. It is characterized by an envelope of increased convection several thousand kilometers across, colocated with regions of anomalous tropospheric water vapor. The convective anomalies are coupled to planetary-scale circulation anomalies that resemble the Matsuno-Gill [*Matsuno*, 1966; *Gill*, 1980] response to an equatorial heat source. This large-scale couplet of circulation and convection propagates eastward at $\sim$5 m s^{-1}, with widespread influences on weather patterns across the globe [*Zhang*, 2013, and references therein]. As a result, it is of global interest to understand the fundamental dynamics that drive the MJO and be able to predict its behavior.

The topic of how increasing tropospheric temperatures in association with increasing carbon dioxide (CO_2) concentrations affect the MJO has gathered more attention throughout the years. *Slingo et al*. [1999] found

that MJO activity is highly dependent on tropical sea surface temperatures, where higher MJO activity occurs when SSTs are higher. They hypothesized that the MJO may strengthen as greenhouse gas concentrations increase. *Jones and Carvalho* [2011] found that MJO activity has been increasing throughout the 20th century, and estimated that MJO activity will increase by ∼50% by the middle of the 21st century. Subsequent modeling studies have found more intense MJO activity as the climate system warms [*Caballero and Huber*, 2010; *Liu et al*., 2013; *Arnold et al*., 2013, 2015; *Subramanian et al*., 2014; *Chang et al*., 2015; *Song and Seo*, 2016; *Carlson and Caballero*, 2016; *Pritchard and Yang*, 2016].

While all these studies have found a link between MJO intensity and activity and increasing greenhouse gases, the physical mechanisms under which the MJO intensifies remain poorly understood. While many studies have shown that the MJO exhibits increased eastward propagation [*Arnold et al*., 2013, 2015; *Chang et al*., 2015; *Pritchard and Yang*, 2016], a quantitative explanation based on theory has not been offered. Furthermore, the relationship between the MJO and the climatological mean state has not been carefully analyzed.

In this study, which comprises two companion papers, we will seek to further our understanding of how the structure and propagation of the MJO changes with increasing CO_2 concentrations using linear analysis and theoretical consideration. We will make use of simulations with different CO_2 concentrations from the NASA Goddard Institute of Space Studies (GISS) global climate model (GCM) as the main tool of analysis. In this first part, we document the changes in the climatological mean state, tropical variability, and MJO structure and propagation. A companion paper analyzes changes in the MJO maintenance and propagation through a comprehensive analysis of moist static energy, the moisture-precipitation relationship and a quantitative analysis from the perspective of moisture mode theory [e.g., *Sobel and Maloney*, 2012, 2013; *Adames and Kim*, 2016].

This paper is structured as follows. The following section describes the model and the method of analysis. Section 3 covers the changes in the model mean state with increasing CO_2. Section 4 describes changes in tropical variability with increasing CO_2. Section 5 documents changes in MJO structure and propagation with increasing CO_2. A concluding discussion is offered in section 6.

2. Data and Methods

2.1. GISS Model Simulation

To investigate the effect of CO_2 changes on the characteristics of the MJO, an atmospheric GCM coupled with a mixed layer ocean model is used. The atmospheric GCM is the atmospheric component of the NASA GISS Model E2 [*Schmidt et al*., 2014]. Since GISS Model E2 was used for CMIP5 [*Taylor et al*., 2012], several important modifications have been made in the model parameterizations, which were shown to improve the model performance. Specifically, changes were made to the convective parameterization toward an increased sensitivity of simulated convection to environmental humidity [*Kim et al*., 2012; *Del Genio et al*., 2012]. These changes, which include stronger lateral entrainment rate and convective rain reevaporation, led the GISS Model E2 to be able to simulate an improved MJO relative to the CMIP5 version [*Kim et al*., 2012; *Del Genio et al*., 2012]. The so-called "post-CMIP5" version of the GISS GCM was formulated by incorporating these changes to the convective parameterization [*Kim et al*., 2012] as well as changes to the convective downdraft and stratiform clouds that mitigate the typical degradation of the mean climate that often accompanies parameterization changes that produce an MJO [*Del Genio et al*., 2012]. Recent improvements to the boundary layer scheme [*Yao and Cheng*, 2012] were also included. The post-CMIP5 version of NASA GISS GCM is employed in the current study.

For the mixed layer ocean model, the ocean heat convergence was first obtained from a fixed-SST simulation, in which observed SST was prescribed as the boundary condition. The ocean heat convergence is then prescribed to the mixed layer ocean model in a series of long-term simulations, in which CO_2 concentrations were varied. Four simulations with 0.5, 1, 2, and 4 times the current level of CO_2 were conducted at a 2.5° (longitude) × 2.0° (latitude) × 40 (levels) resolution, and with a depth of the mixed layer 65 m. After reaching an equilibrium (i.e., steady global mean surface temperature), each experiment was carried out for additional 30–50 years, and the daily mean data from the last 20 years of simulations are used in the current study.

We make use of the following model output fields in this study. The horizontal wind components (u, v) are used as field variables, as well as vertical velocity (ω). Specific humidity (q), temperature (T), and geopotential height (Z) are also used as field variables and in the calculation of dry and moist static energies. Temperature is also used in the calculation of the saturation specific humidity (q_s) and relative humidity (q/q_s). Other variables that we use include precipitation (P), and outgoing longwave radiation (OLR). The Eulerian temporal tendency of moisture, $\partial q/\partial t$ is calculated by taking a 2 day centered difference of q.

Many of the fields described in this study correspond to intraseasonal anomalies, obtained by removing the mean and first three harmonics of the annual cycle based on the 20 year simulation. Additionally, a 101 point Lanczos filter [*Duchon*, 1979] is used to retain anomalies within the 20–100 day time scale. Some of the fields are "MJO-filtered" anomalies, which, in addition to being filtered over the 20–100 day time scale, they are filtered to retain only the eastward-propagating, zonal wave number 1–5 signal, based on the protocol of *Hayashi* [1981].

2.2. Methods

Many of the results shown in this study are obtained through linear regression analysis, obtained following the methods described in *Adames and Wallace* [2014], which makes use of the following matrix operation

$$\mathbf{D}=\mathbf{S}\hat{\mathbf{P}}^{\top}/N$$

where $\mathbf{D}$ is the linear regression for a two-dimensional matrix $\mathbf{S}$, corresponding to a field variable S. The matrix $\mathbf{S}$ is two-dimensional since the field variable S is reshaped so that its spatial dimensions are contained in the rows of the matrix $\mathbf{S}$ [i.e., $\mathbf{S}=\mathbf{S}(x\times y\times p,t)$]. The regression map is obtained by projecting $\mathbf{S}$ upon a standardized MJO index, $\hat{\mathbf{P}}$, and dividing by the number of days, N. The regression patterns shown later (e.g., Figure 9) correspond to linear regressions upon an MJO-filtered time series of OLR, averaged over the western Pacific basin (15°N/S 140°E–180°E). This region corresponds to the location of strongest intraseasonal variability in the model simulations. We have verified that the results presented in this study are reproducible using time series corresponding to other regions of the Indo-Pacific warm pool (60°E–180°E) as well as by using EOF analysis. Contour and shading intervals in the plots presented here are scaled to the approximate value of the 95% confidence interval based on a two-sided t test.

For the scatterplots shown in Figures 6, 7, and 13, we calculated a range of uncertainty corresponding to the 95% confidence interval subsampling the time series of each variable. We did this by creating a 10 member ensemble composed of 5 year time series, randomly selected from the 20 year time series. For plots of MJO-filtered anomalies, the ensemble also includes members in which the zonal wave numbers retained in the MJO filter varied, with 10 members retaining only zonal wave numbers 1–4, 1–5, up to zonal wave numbers 1–10, for a total of 70 members. We have varied the length of the time series or the amount of members in the ensemble and found no change in the error bars presented here.

Space-time spectral analysis is performed in section 4 of this study, following the methods of *Wheeler and Kiladis* [1999], *Masunaga* [2007], and *Hendon and Wheeler* [2008]. Time series of precipitation and column water vapor are divided into 180 day segments that overlap by 90 days, as in *Waliser et al*. [2009] and *Kim et al*. [2009]. Then, the space-time mean and linear trends are removed by least squares fits and the ends of the series are tapered to zero through the use of a Hanning window. After tapering, complex fast Fourier transforms (FFTs) are computed in longitude and then in time. Finally, the power spectrum is averaged over all segments and over the 15°N–15°S belt. The number of degrees of freedom is calculated to be 81 [2 (amplitude and phase) $\times$ 20 (years) $\times$ 365 (days)/180 (segment length)]. The signal strength is calculated as $(P_{xx}-P_{red})/P_{xx}$, where P_{red} is the red spectrum, calculated analytically using equation (1) of *Masunaga* [2007], and values above 0.5 are considered to be statistically significant in this study. We will focus on showing only equatorially symmetric component [*Yanai and Murakami*, 1970], where the MJO signal is strongest, and to facilitate comparison with other studies. Additionally, the power spectrum is used to calculate the east-west power ratio [*Sperber and Kim*, 2012], which is defined here as the ratio of intraseasonal eastward versus westward propagating spectral power (k = 1–5, 20–100 day time scale).

In the time-longitude lag regression plots shown in section 5, we estimate the phase speeds and group velocities of the MJO using OLR, precipitation and column water vapor. These calculations are performed following the method described in *Adames and Kim* [2016]. For the phase speed calculation, we choose

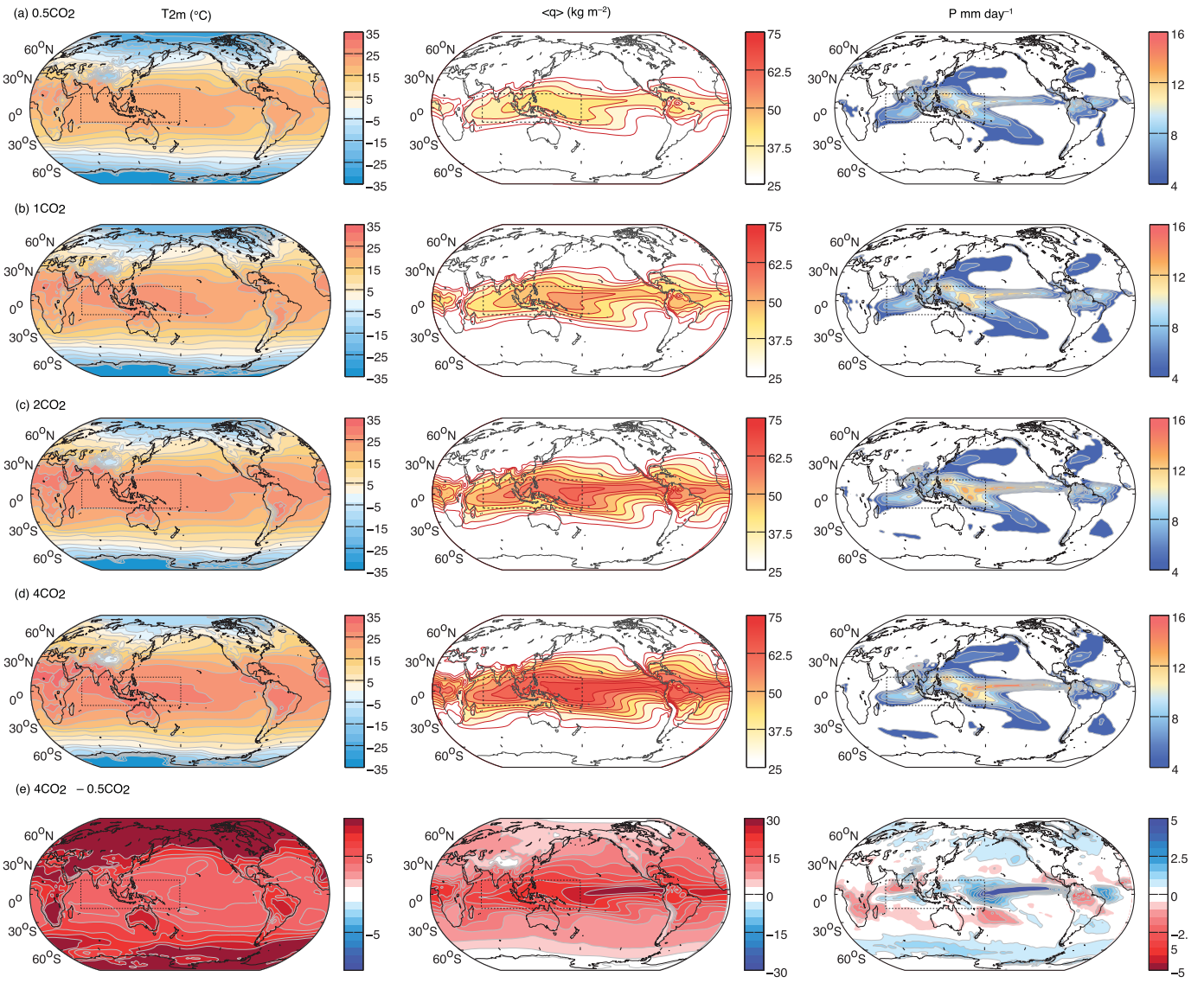

Figure 1. (left) Mean November-April (NDJFMA) surface temperature, (middle) column water vapor, and (right) precipitation for the (a) $0.5CO_2$, (b) $1CO_2$, (c) $2CO_2$, and (d) $4CO_2$ GISS model simulations. The difference between the $4CO_2$ and $0.5CO_2$ simulations is shown in Figure 1e.

extrema (maxima and minima) that occur within 25 days of the reference time (lag day 0). The phase speeds are calculated for each time-longitude section by averaging the MJO-filtered anomaly fields across the longitude intervals ranging from 130°E to 145°E, 145°E to 160°E, 160°E to 175°E, and 175°E to 190°E. For each field, the time when a statistically significant extremum occurs is calculated within each longitude band. Phase speed is then calculated by linear least squares fit of the time in which an extremum occurs within each longitude band. If multiple propagating envelopes are found, the phase speed is estimated by averaging all of them.

The group velocities are calculated in a similar manner. We calculate the zonal and temporal position of each local extremum. A local extremum is defined here as a local maximum/minimum occurring within 25 days of the reference time. For a local maximum/minimum to be considered, it must be the largest anomaly in space and time within an interval of 10 days and be significant at the 95% confidence interval. After all the local extrema are identified, the group velocity is calculated through a linear least squares fit in the longitude-time space.

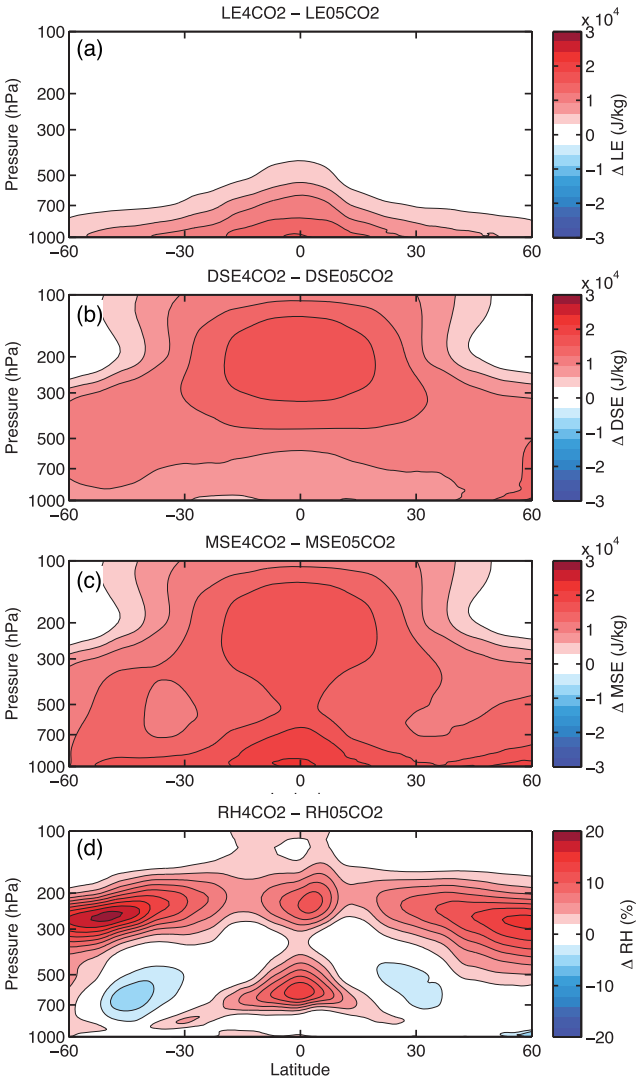

Figure 2. Differences between the $4CO_2$ and $0.5CO_2$ simulation NDJFMA zonally averaged (a) latent energy L_{vq}, (b) dry static energy $s=C_pT+gZ$, (c) moist static energy $m=L_vq+s$, and (d) relative humidity q/q_s.

3. Mean State Changes With Increasing CO_2

In order to get an overview of the mean state of the four simulations, the left column of Figure 1 shows global distributions of annual mean surface temperatures for the four GISS simulations. An approximately linear increase in surface temperatures is observed with each doubling in CO_2 concentration. The annual mean column-integrated moisture $\langle q \rangle$ and precipitation P fields are shown in the middle and right columns of Figure 1, respectively. A sharp increase in column moisture is evident at all geographical locations, but in contrast to temperature changes that exhibits the so-called polar-amplification, moisture increases more over the tropics, consistent with the Clausius-Clapeyron equation. It is noteworthy that column moisture increases the fastest over the central and eastern Pacific ITCZ. Unlike moisture, which increases everywhere with warming, not all locations exhibit increasing precipitation. Instead, precipitation increases the most over the eastern and central Pacific, consistent with the strongest increments in moisture and consistent with a weakening of the Walker Circulation with increasing CO_2 [*Seager et al.*, 2010]. It is worth noticing that precipitation decreases over tropical landmasses.

Latitude-height cross sections of the difference in zonally averaged latent energy (L_{vq}, where $L_v=2.5\times10^6$ J kg^{-1} is the latent heat of vaporization), dry and moist static energy, and relative humidity between the $0.5CO_2$ and $4CO_2$ runs are shown in Figure 2. An increase in lower-tropospheric latent energy is observed at all latitudes, with a maximum near the equator, consistent with Figure 1. Dry static energy, defined as $s=C_pT+gZ$, where $C_p=1004$ J K^{-1} is the specific heat of dry air, increases at all heights and latitudes. Unlike moisture, s has a maximum rate of change near the equator at ~200 hPa, indicating an increase in static stability with warming. Moist static energy (MSE, $m=L_vq+s$) increases the most near the surface at the equator, consistent with the sharp increase in specific humidity near the surface. A secondary maximum is observed ~200 hPa where the dry static energy anomalies are a maximum. Even though latent energy L_vq increases the most over the lower troposphere, relative humidity, shown in Figure 2d increases over the tropical lower free troposphere ~500–750 hPa and just below the tropopause ~200–300 hPa.

In order to quantify the trends in mean moisture and precipitation, scatterplots of column moisture, precipitation, and column relative humidity, averaged over the equatorial warm pool (60°E–180°E, 15°N/S the region is enclosed by dotted lines in Figure 1), where MJO activity is strongest, are shown in Figure 3 as a function of the mean tropical temperature. Only points located over the oceans are included. Column moisture increases at a rate of ~7.1% K^{-1}, similar to that predicted by the Clausius-Clapeyron equation, while

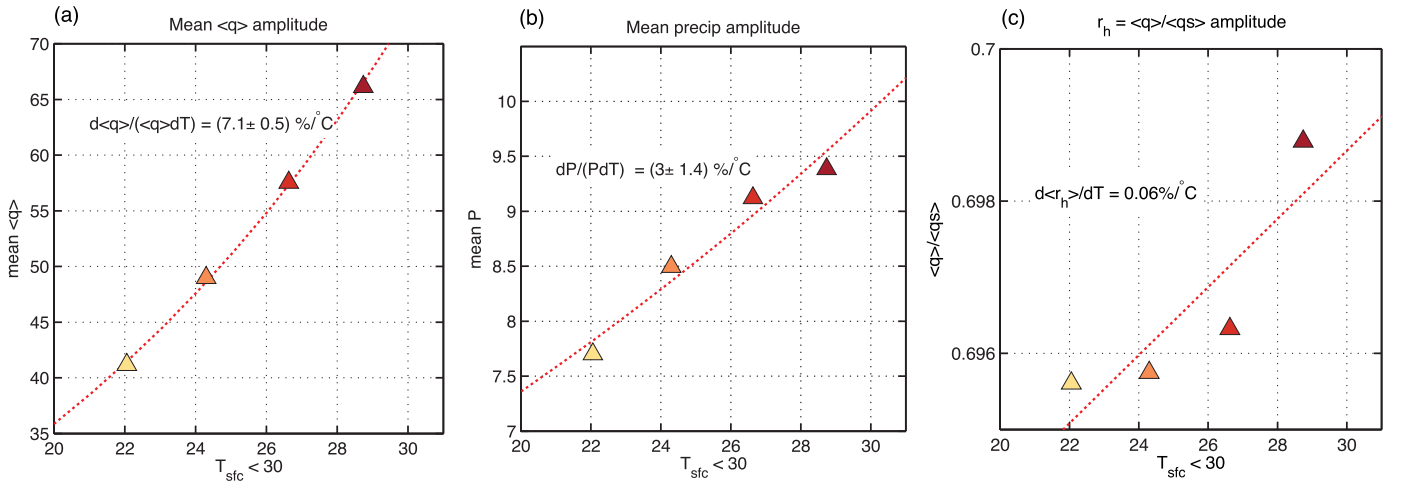

Figure 3. Scatterplots showing NDJFMA mean, warm pool averaged (60°E–180°E, 10°N/S) (a) column water vapor $\langle q \rangle$, (b) precipitation, and (c) column relative humidity as a function of the mean surface temperature averaged over the 30°N/S latitude belt. The dashed line in each plot corresponds to the nonlinear least squares fit of the trend in each variable.

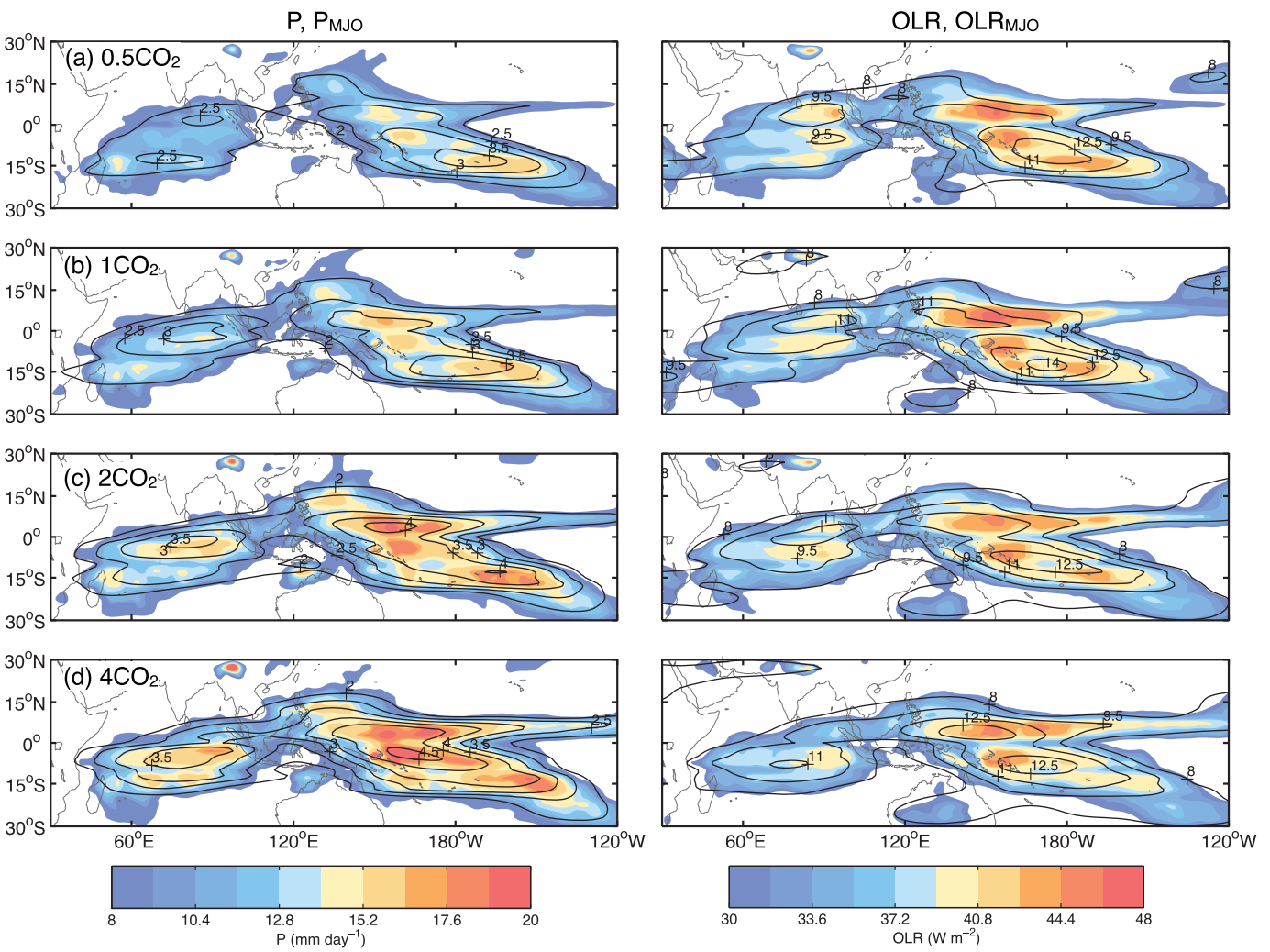

Figure 4. Standard deviation of the NDJFMA anomalous precipitation (shaded left) and MJO-filtered (contoured left) precipitation, and anomalous OLR (shaded right) and MJO-filtered OLR (contoured right) for the (a) $0.5CO_2$, (b) $1CO_2$, (c) $2CO_2$, and (d) $4CO_2$ simulations.

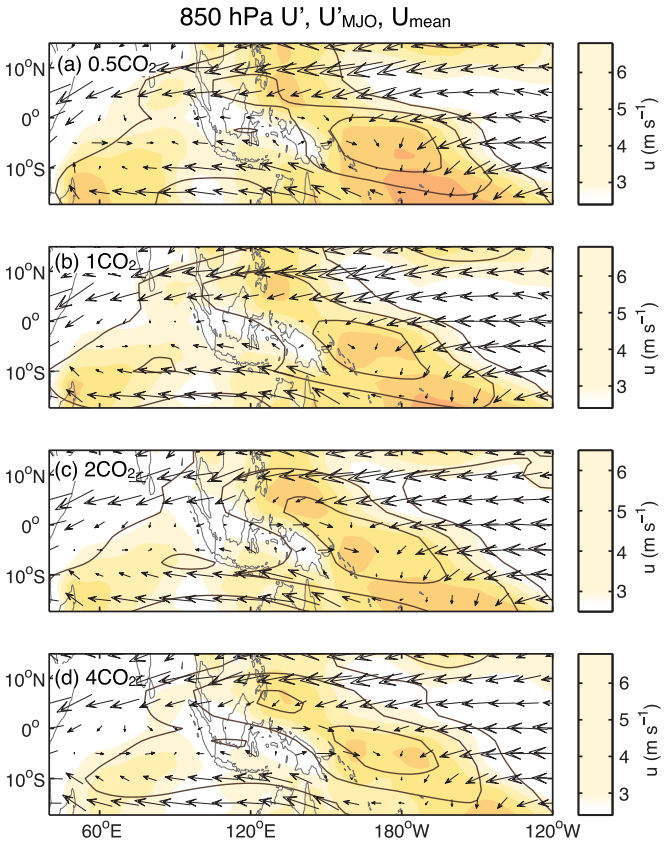

Figure 5. Standard deviation of NDJFMA 850 hPa zonal wind anomalies (shaded) and MJO-filtered zonal wind anomalies (contoured). The arrows correspond to the NDJFMA climatological mean 850 hPa flow. The longest arrows correspond to ~ -7 m s^{-1}. Contour interval is 0.25 m s^{-1} starting at 1 m s^{-1}.

precipitation increases at a fraction of this rate ($\sim$3% K^{-1}). Global precipitation increases at a smaller rate than water vapor because it is highly constrained by the global radiative cooling rate [*Allen and Ingram*, 2002; *Held and Soden*, 2006; *O'Gorman et al*., 2012; *Pendergrass and Hartmann*, 2014]. The rate of change of warm-pool averaged precipitation is consistent with this notion, augmented by changes in the mean warm pool circulation with increasing CO_2 [*Chou et al*., 2009; *Seager et al*., 2010]. In contrast, column relative humidity ($R_h = \langle q \rangle / \langle q_s \rangle$), shown in the right plot of Figure 3, shows little change as temperatures increase over the warm pool.

4. Changes in Warm Pool Variability With Increasing CO_2

Maps of the standard deviation of daily precipitation and OLR are shown in Figure 4. Variability in precipitation exhibits a peak over the SPCZ in the 0.5CO_2 run, while OLR peaks over the western Pacific. As CO_2 increases, variability in precipitation amplifies and the peak shifts to the western Pacific near the maximum in OLR variability. A significant amplification in precipitation is also observed over the Indian Ocean and over the ITCZ, consistent with results of *Wolding et al*. [2017]. In contrast, OLR variability shows a slight decrease in variability. MJO-filtered variability, shown in contours, shows similar trends in both fields. These results are qualitatively consistent with Table 1 of *Arnold et al*. [2015], which shows that precipitation variance increases at a faster pace than OLR variance.

Maps of the standard deviation of zonal wind are shown in Figure 5. A slight decrease in variability is observed, similarly to the OLR field. When only the MJO spatial and temporal scales are considered, a trend is not entirely clear, with a decrease in amplitude over the Indian ocean, but relatively little change over the Maritime Continent and the western Pacific. Similar results were found for zonal wind variability in the upper troposphere (not shown). The climatological-mean winds, shown as arrows in Figure 5, do not show any clear trend either.

In order to quantify the changes in variability over the Indo-Pacific warm pool, scatterplots as in those shown in Figure 3 but for the standard deviation of anomalous column water vapor $\langle q \rangle$ and precipitation P are shown in Figure 6. Interestingly, for both precipitation and column water vapor, the changes in variability scales well with those of the mean states (bottom plots of Figure 6), consistent with the results of *Pritchard and Yang* [2016]. In other words, the moisture and precipitation variability increases at a same rate with which the climatological mean values increase, suggesting that mean state changes might constrain changes in variability. In contrast to variability across all temporal and spatial scales, MJO-filtered variability in moisture and precipitation, shown in Figures 7a and 7b, increases at a faster rate than variability across all spatial and temporal scales. Although not discussed, results in Table 1 of *Arnold et al*. [2015] suggest that MJO variability increases at a higher rate than total

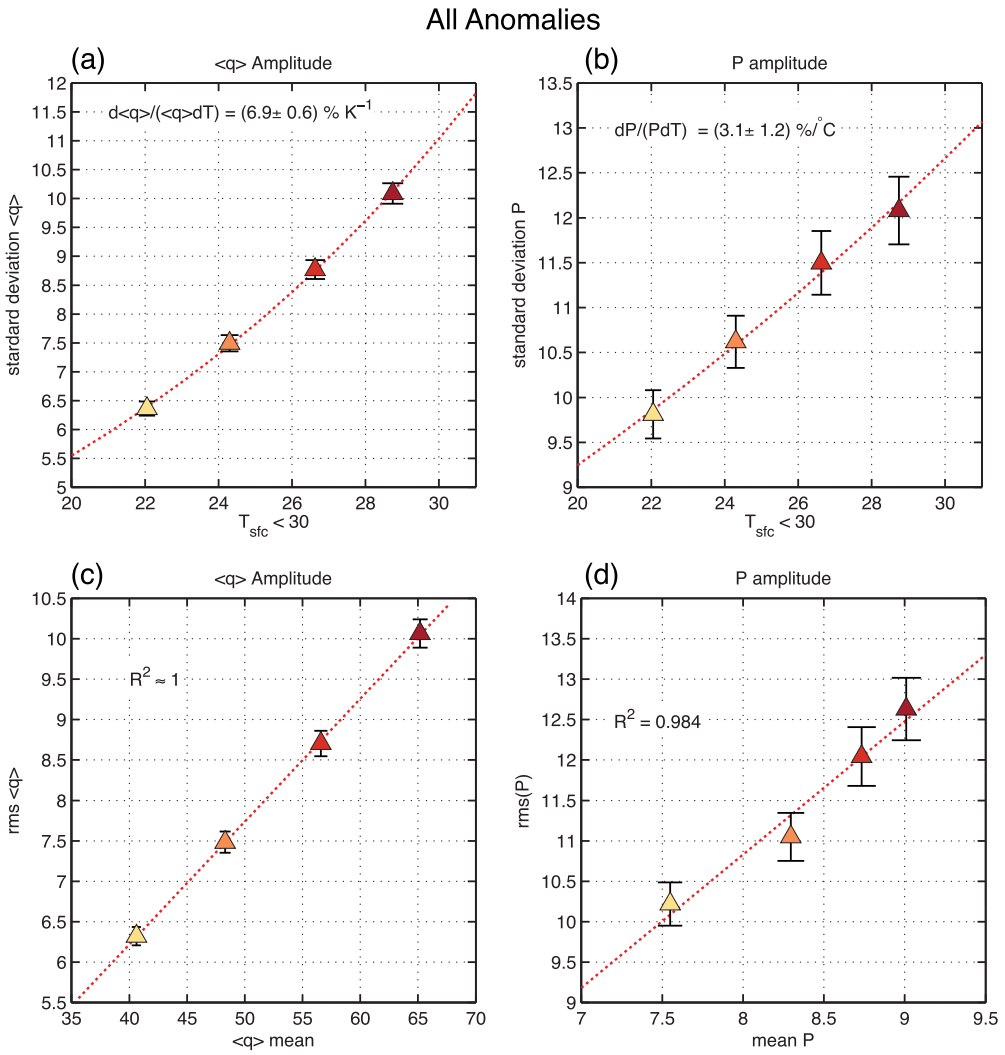

Figure 6. Scatterplots showing NDJFMA, warm pool averaged (60°E–180°E, 10°N/S) standard deviation of column water vapor $\langle q \rangle$ (left) and precipitation (right) as a function of tropical surface temperature (top) and NDJFMA-mean moisture and precipitation (bottom). The dashed line in each plot corresponds to the nonlinear least squares fit of the trend in each variable. The percentage change of the anomalies per degree of warming is shown in the top plots, and the correlation coefficient between the NDJFMA standard deviation and mean is shown in the bottom plots. Error bars correspond to the spread that arises from subsampling the time series of each variable.

variability in SP-CESM as well, with MJO variance increasing 56% between their control and 4CO_2 runs, while total variability increases 41%.

No clear change in MJO-related zonal wind variability is seen (Figure 7c). This result is consistent with the findings of *Arnold et al.* [2015] (see their Table 1), *Maloney and Xie* [2013] and *Wolding et al.* [2017]. *Maloney and Xie* [2013] and *Wolding et al.* [2017] suggested that this trend is due to an increase in tropical dry static stability with warming, which acts to weaken zonal wind variability. Increasing static stability acts to negate any increase in zonal wind variability due to increasing amplitude in precipitation. The role that increasing precipitation and static stability play on the MJO will be further discussed in part II.

A more comprehensive understanding of how variability in the model is changing with increasing CO_2 can be obtained by performing a space-time spectral analysis over the equatorial belt. Column (1) of Figure 8 shows the zonal wave number-frequency power of column water vapor averaged over the 15°N/S belt. An increase in spectral power is observed at all frequencies and wave numbers as CO_2 increases, consistent

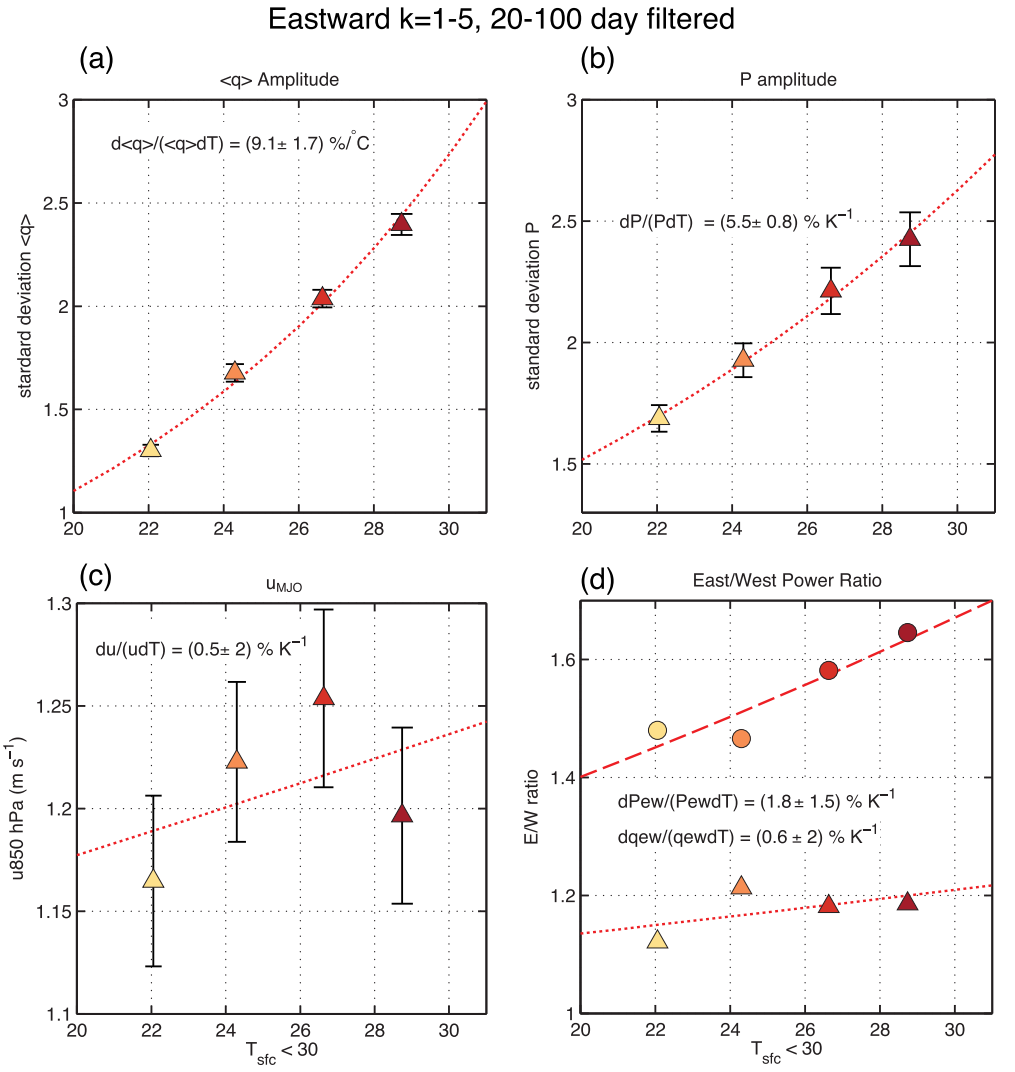

Figure 7. Scatterplots showing NDJFMA, MJO-filtered standard deviation of (a) column water vapor $\langle q \rangle$ and (b) precipitation, and (c) 850 hPa zonal wind as a function of tropical surface temperature. All fields are averages over the warm pool (60°E–180°E, 10°N/S) (d) East-west power ratio of precipitation (circles) and column water vapor (triangles) for the four GISS simulations. The east-west power ratio is calculated as the ratio in spectral power between eastward-propagating wave number averaged over zonal wave numbers 1–5 and 20–100 day time scales. The percentage-based rate of changes is shown in the figure. The dashed line in each plot corresponds to the nonlinear least squares fit of the trend in each variable. Error bars correspond to the spread that arises from varying the zonal wave numbers retained in the MJO filter (varying from retaining zonal wave numbers 1–3 to 1–10) and from subsampling the time series.

with the overall increase in variability shown in Figure 6. However, the amplification is strongest along the lowest frequencies and zonal wave numbers, suggesting a systematic "reddening" of tropical water vapor variability with increasing CO_2. This reddening is more clearly depicted in the difference in the power spectrum between the $4CO_2$ and $0.5CO_2$ simulations, shown in Figure 8e. This systematic reddening of the column moisture power spectrum may explain why intraseasonal variations in moisture (Figure 7a) increase at a faster rate than other spatial and temporal scales. The spectrum of precipitation (column 5) exhibits a more uniform change in spectral density than water vapor does. A reddening of this spectrum is not as clear as changes are dominated by a strengthening of spectral power along the Kelvin wave dispersion curve.

Figure 7d shows the east-west power ratio of precipitation and column water vapor for the four simulations analyzed here. If the MJO were strengthening at a faster rate than the background spectrum, we would expect the east-west power ratio to increase with increasing CO_2. However, the trends are weaker than those of MJO-filtered anomalies, indicating that the amplification occurs across broad intraseasonal bands,

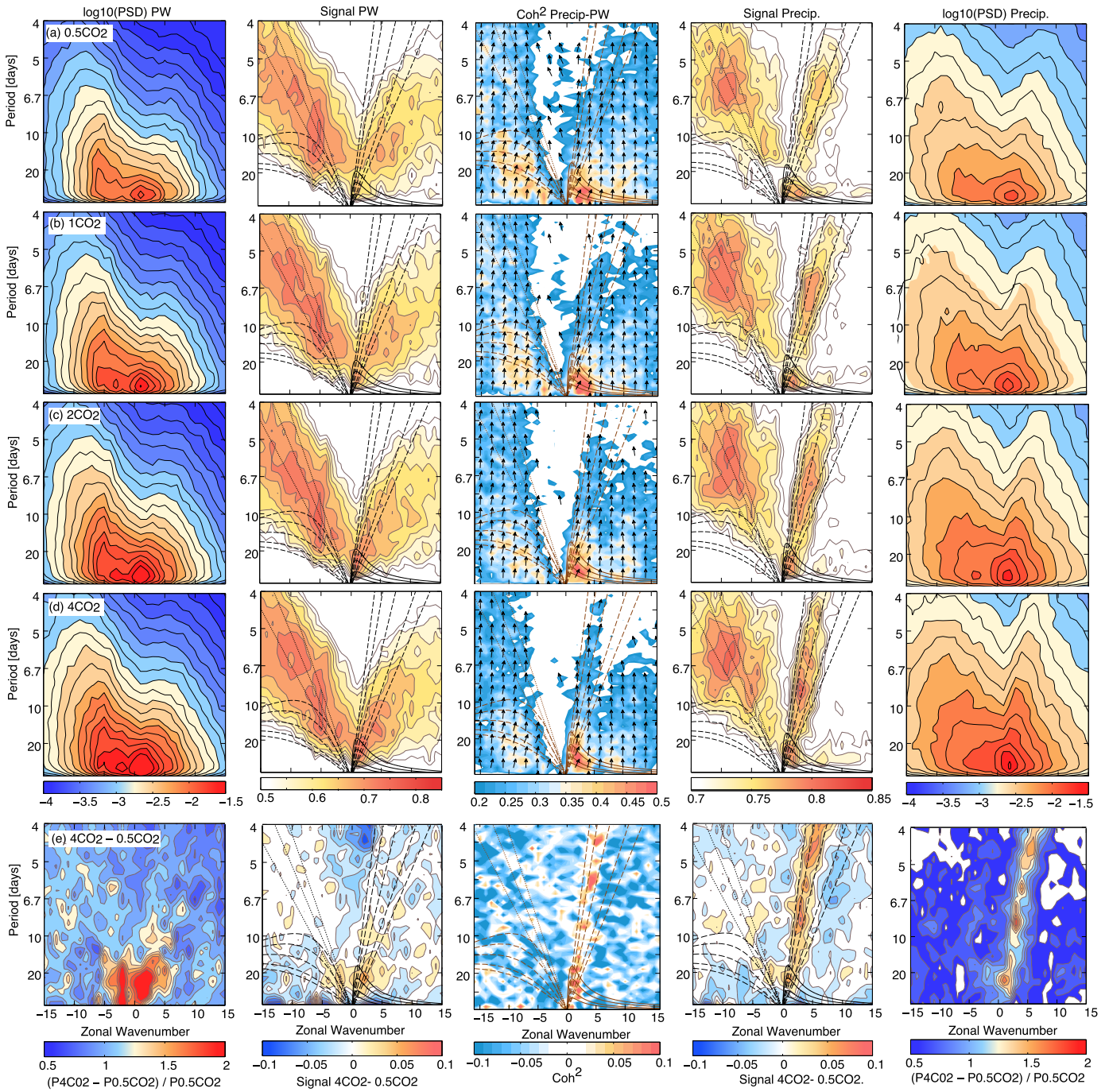

Figure 8. Space-time spectral analysis of column water vapor $\langle q \rangle$ and precipitation P: (1 and 5) normalized power spectrum of the symmetric component of $\langle q \rangle$ and P, respectively, over the 15°S–15°N latitude band. (2 and 4) Signal strength of $\langle q \rangle$ and precipitation P, respectively. (3) Coherence squared (shading) and phase angle (arrow) between $\langle q \rangle$ and precipitation P. Upward-pointing vector corresponds to a zero phase lag, downward implies out of phase, rightward implies that $\langle q \rangle$ leads P by a quarter cycle, and leftward implies $\langle q \rangle$ lags P by a quarter cycle. The rows show the spectral analysis corresponding to the (a) $0.5CO_2$, (b) $1CO_2$, (c) $2CO_2$, and (d) $4CO_2$ simulations, and (e) the difference between the $4CO_2$ and $0.5CO_2$ simulations. Dispersion curves are plotted in columns (2)–(4) for Kelvin and $n = 1$ equatorial Rossby waves, with equivalent depths of 12, 25 50, and 90 m, respectively. Dotted lines indicate constant phase speeds of 7.0, 9.0, and 11.0 m s^{-1}, which are representative of westward-propagating tropical depression and easterly waves [see also *Yasunaga and Mapes*, 2012]. Contour interval is every 0.05 signal strength fraction beginning at 0.5. The solid lines correspond to MJO dispersion curves as derived in equation (29a) in *Adames and Kim* [2016].

not preferentially in the eastward-propagating, planetary-scale waves (i.e., MJO). This suggests that part of the MJO amplification is due to overall increase in tropical variability, especially in the intraseasonal components, consistent with the notion of a reddening spectrum as seen in Figure 8e. The east-west ratio values for precipitation found here are smaller than those found by *Arnold et al.* [2015]. Their study found a east-

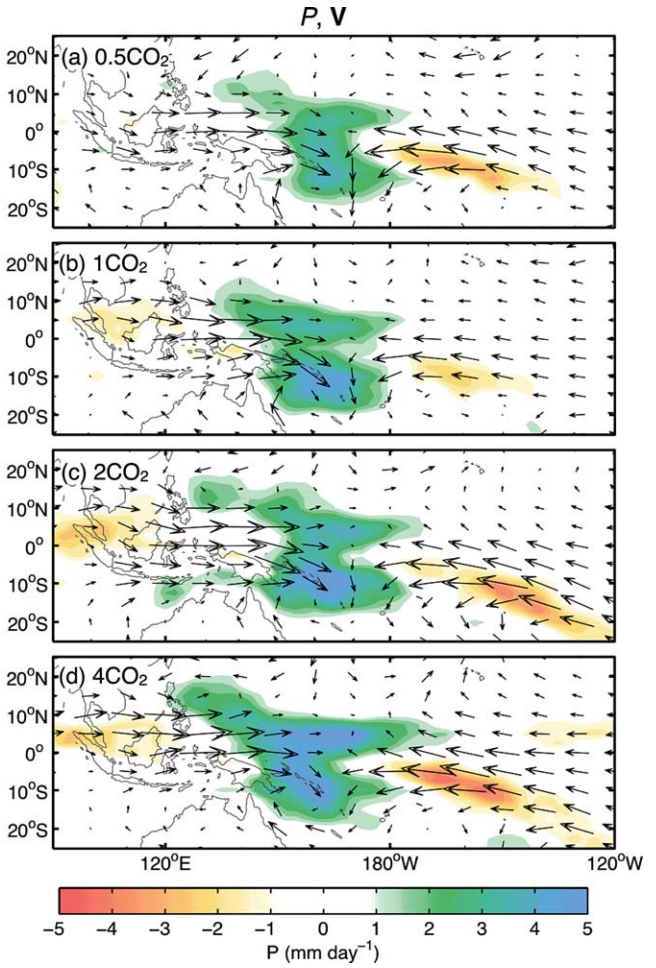

Figure 9. Linear regression for precipitation (shaded) and 850 hPa wind anomalies (arrows) onto an MJO-filtered time series centered over the western Pacific. Each plot corresponds to the anomaly fields for the (a) $0.5CO_2$, (b) $1CO_2$, (c) $2CO_2$, and (d) $4CO_2$ simulations. The largest arrows correspond to wind anomalies of $\sim$1 m s^{-1}.

west ratio that increased from 1.67 in their $1CO_2$ to 2.20 in their $4CO_2$, an increase of roughly 30%, nearly three times the rate of change found here. Changes in the spectral variance at intraseasonal time scales in *Chang et al.* [2015], *Carlson and Caballero* [2016], and *Pritchard and Yang* [2016] also suggest an increasing east-west ratio, although exact rates of change were not provided in those studies.

Columns (2) and (4) of Figure 8 show the signal strength of water vapor and precipitation, respectively, defined as in *Hendon and Wheeler* [2008] as the amount of signal that lies above a red noise spectrum, $S=(P_{xx}-P_{red})/P_{xx}$. The plots are overlaid by the dispersion curves for Kelvin, $n=1$ equatorial Rossby, tropical depression-type disturbances as defined by *Yasunaga and Mapes* [2012], and for the MJO, as defined in equation (29a) of *Adames and Kim* [2016] (curves are defined in the same way as their Figure 13). For precipitation, the strongest signal in the MJO band is found between zonal wave numbers 1–5 in the $0.5CO_2$ simulation, with some signal occurring at higher wave numbers. The MJO signal in water vapor is confined within the first three zonal wave numbers and slightly shifted toward higher frequencies. While precipitation exhibits a pronounced Kelvin wave signal, such a signal is largely absent in the column water vapor signal, consistent with previous studies [*Sobel and Bretherton*, 2003; *Yasunaga and Mapes*, 2012]. However, it is noteworthy that an eastward-propagating signal in $\langle q \rangle$ is seen that is reminiscent of Kelvin waves of shallower equivalent depths. This signal is more pronounced than what is seen in observations [Figure 1e of *Yasunaga and Mapes*, 2012].

As CO_2 concentrations increase, the precipitation signal becomes more confined at wave numbers 1–3 and shifts toward higher frequencies. The difference in signal for both column water vapor and precipitation is shown in the bottom plot of Figure 8. For both fields, an increase in signal is seen over the 20–40 day time scale, while a reduction is seen at lower frequencies. This is consistent with the MJO shifting toward higher frequencies in warmer climates [e.g., *Arnold et al.*, 2013; *Pritchard and Yang*, 2016]. It is noteworthy that *Arnold et al.* [2013] and *Pritchard and Yang* [2016] also found these trends in spite of using different models and different basic state configurations. A strengthening of the Kelvin wave signal in precipitation is observed, combined with a shift toward larger equivalent depth, consistent with the increasing static stability seen in Figure 2b. However, that no clear Kelvin wave signal is apparent along the water vapor dispersion curves is in agreement with the notion that precipitation in relation to Kelvin wave activity is mainly due to changes in tropospheric temperature with secondary effects from moisture fluctuations [*Sobel and Bretherton*, 2003; *Raymond and Fuchs*, 2009; *Herman et al.*, 2016].

Coherence squared and the spectral phase angle between the precipitation and column moisture fields is shown in column (3) of Figure 8. A strong correspondence is observed between the largest coherence

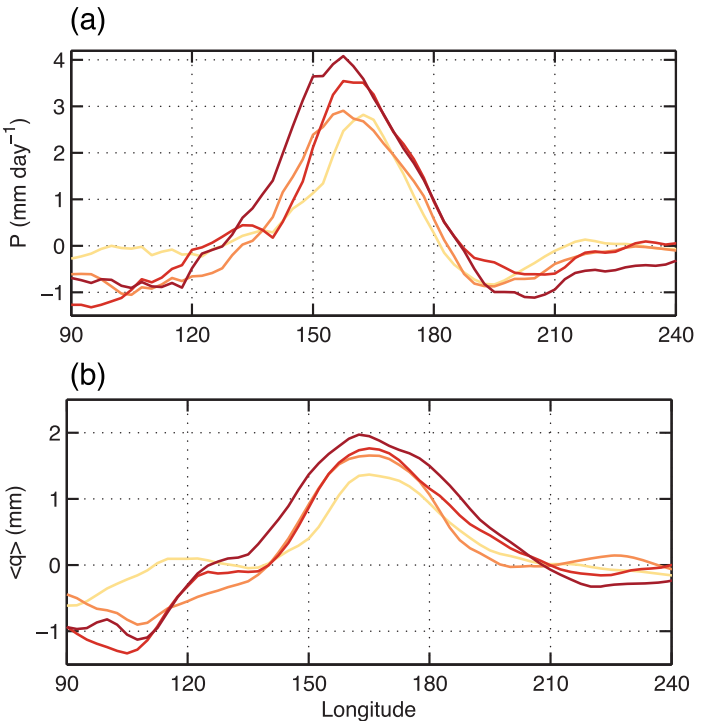

Figure 10. Linear regression for (a) precipitation and (b) column-integrated water vapor regressed onto an MJO-filtered time series centered over the western Pacific and averaged over the 10°N/S latitude belt. The yellow line corresponds to the $0.5CO_2$ simulation, the orange line to the $1CO_2$, light red to $2CO_2$ and dark red to $4CO_2$.

values and the dispersion curves corresponding to the MJO. The high values of coherence along the MJO band are colocated with the MJO-related precipitation signal in column (4) of Figure 8. Coherence values along the dispersion curves corresponding to other wave modes are much smaller than those seen along the MJO band. As CO_2 concentrations increase, the magnitude of the coherence does not significantly change, but becomes more concentrated at the lowest zonal wave numbers. There is also indication of a shift toward higher frequency, with red shading, corresponding to the largest coherence values, seen near the 20 day time scale band near zonal wave number 1. This change is most clearly seen in plot (e), with the difference of coherence between the 0.5 and $4CO_2$ runs showing increased coherence along zonal wave number 1, and decreased coherence along higher zonal wave numbers. The spectral phase angle, shown as arrows, indicates that column moisture slightly leads the precipitation anomalies, consistent with observations [*Yasunaga and Mapes*, 2012]. No significant change in the phasing between water vapor and precipitation with warming is observed.

5. Changes in the MJO Characteristics With Increasing CO_2

In order to elucidate the changes in the structure and propagation of the MJO with increasing CO_2, a linear regression analysis is performed using a time-varying index. We will focus our analysis on maps based on 20–100 day time scale, eastward-propagating wave numbers 1–5 OLR time series averaged over the western Pacific (140°E–180°E, 10°N/S), where intraseasonal variability in the GISS simulations is strongest. We have verified that results shown herein are also quantitatively reproducible using OLR-based time series over the Maritime Continent or the Indian Ocean, or using principal components from EOF analysis.

Regression maps of the precipitation field along with the 850 hPa winds are shown in Figure 9. The structure of precipitation in the western Pacific can be separated into a sector of rainfall that is located along the intertropical convergence zone (ITCZ) ∼7°, and a second maximum centered in the Southern Hemisphere oriented along the south Pacific convergence zone (SPCZ). As CO_2 concentrations increase, the precipitation anomalies in both regions amplify. The anomalies also become more zonally extensive, though the increase in areal extent is most apparent in the separation between the regions of enhanced precipitation and the regions of decreased precipitation (green and orange shading, respectively). Consistent with Figures 5 and 7c, no clear change in the amplitude of the wind anomalies is seen.

Figure 10a shows the precipitation anomalies from Figure 9 meridionally averaged over the 10°N/S latitude belt. An increase in zonal extent is observed, most clearly seen in the separation in the zero crossing between the $0.5CO_2$ and $4CO_2$ simulations. There is also greater separation between the maximum in anomalous precipitation

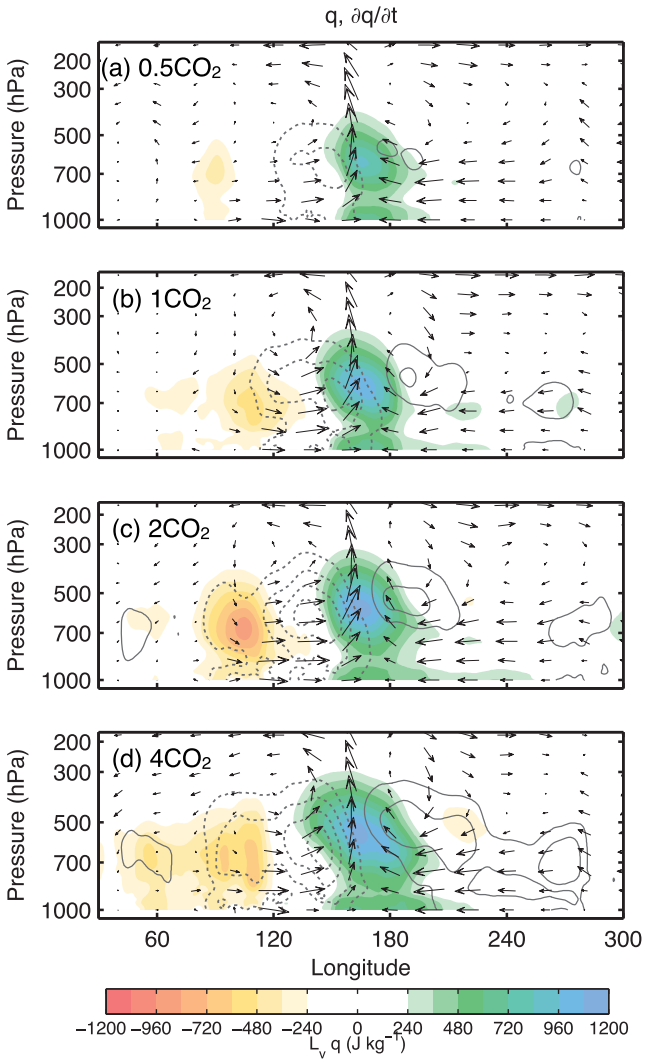

Figure 11. Composite longitude-height cross section of latent energy anomalies $L_v q'$(shaded), its temporal tendency $L_v \partial q'/\partial t$ and the anomalous zonal mass circulation $(\rho u', \rho w')$ for the (a) $0.5CO_2$, (b) $1CO_2$, (c) $2CO_2$, and (d) $4CO_2$ simulations. The largest zonal flux vector is ~0.2 kg m^{-2} s^{-1}. Contour interval 30 J kg^{-1} d^{-1}.

~160° and the minimum to the east ~190°–210°. Column-integrated water vapor, shown in Figure 10b shows this trend even more clearly, particularly to the west of the maximum $\langle q \rangle$ anomalies. However, from these plot alone it is not clear what the rate of change in scale is, or if it occurs abruptly in the 2 and $4CO_2$ simulations.

Longitude-height cross sections of the specific humidity field, and its local temporal tendency $\partial q'/\partial t$ are shown in Figure 11. An amplification of the specific humidity anomalies is clearly evident. Additionally, a deepening of the moisture anomalies is also observed, with the height of the deepest shading in each plot occurring higher in the troposphere as CO_2 concentrations increase. The location of the regions of maximum moistening to the east, and drying to the west are similar to those found by *Chikira* [2014], *Adames and Wallace* [2015], and *Wolding and Maloney* [2015]. The moisture tendency field also shows hints of deepening as CO_2 concentrations increase.

Time-longitude diagrams of $\langle q' \rangle$, precipitation and OLR are shown in Figure 12. These are lag regressions constructed using the OLR time series for the western Pacific sector. Maxima in the three fields (depicted as circles in Figure 12) become progressively more separated from each other, indicative of an increase in the MJO's group velocity. As a result of these changes, the MJO-related anomalies propagate over a larger area of the tropics in a warmer climate. Whereas it propagates from ~120° to 200° of longitude in the $0.5CO_2$ simulation, it propagates from ~60° to 220° in the $4CO_2$ simulation. These results are generally consistent with studies by *Arnold et al.* [2013, 2015] and *Chang et al.* [2015] among others, who also found the MJO to become faster and cover a larger area of the globe as the climate warms.

Quantitative estimates of the changes in MJO shown in Figures 9–12 are shown in Figure 13. Figure 13a shows the mean wave number obtained from spatial spectral analysis of the three fields shown in Figure 12. The decreasing trend seen in Figure 13a is consistent with the larger zonal extent of the moisture and precipitation anomalies seen in Figures 9–12. The scatterplot indicates that the MJO-related moisture and precipitation anomalies are increasing in zonal extent at a rate of approximately ~150 km per degree of tropical warming, and the zonal scale of the anomalies in the $4CO_2$ simulation is roughly 500 km larger in zonal extent than the anomalies in the $0.5CO_2$ simulation. It is noteworthy the MJO's zonal wave number in all four GISS simulations is still larger than observations, which was estimated at 1.81 by *Adames and Kim* [2016]. *Chikira and Sugiyama* [2013] also found that their simulated MJO was smaller in horizontal extent than the observed MJO.

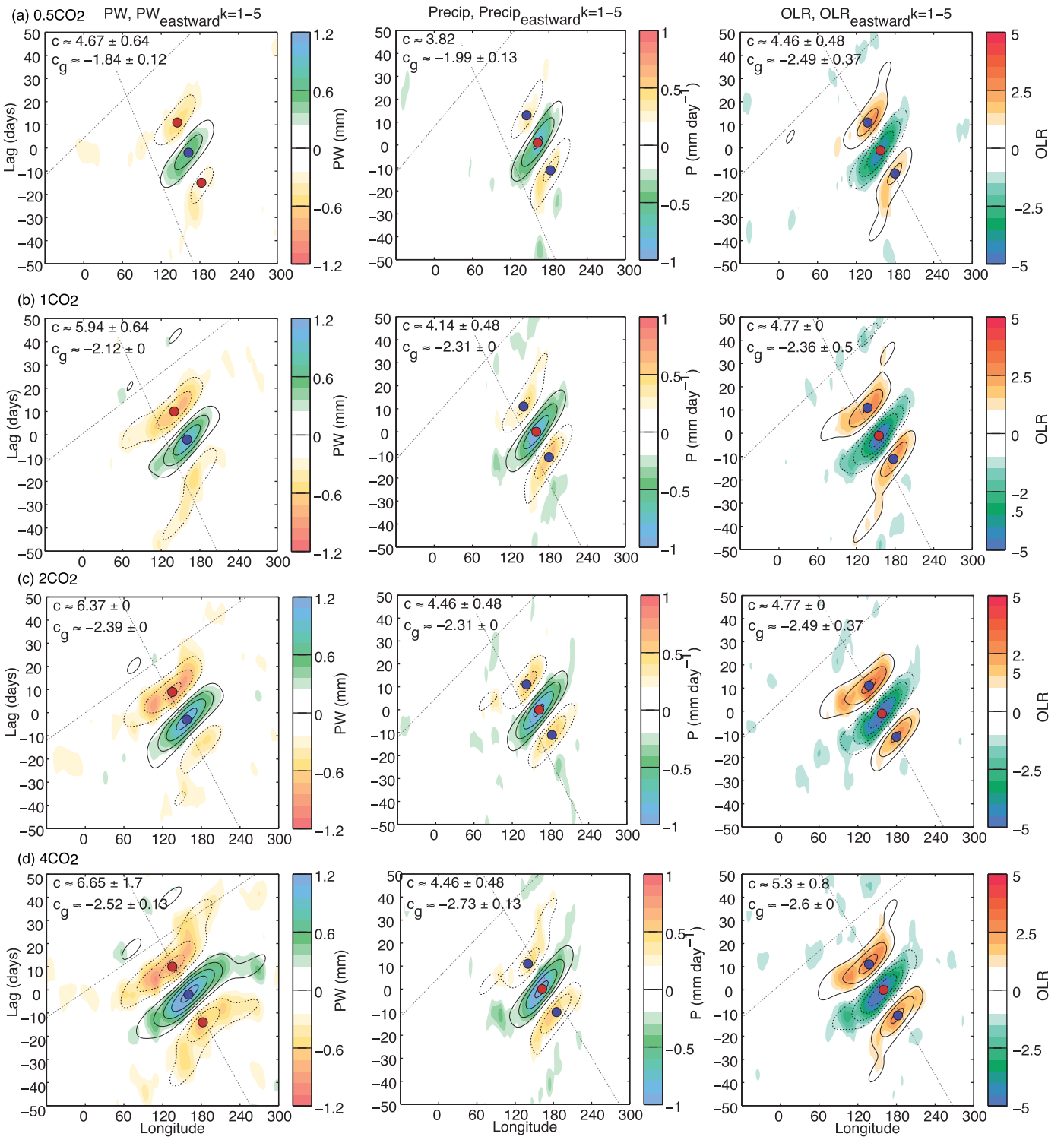

Figure 12. Time-longitude diagrams of 20–100 day time scale filtered (shaded) and MJO-filtered (contours) $\langle q \rangle$ (left column), precipitation (middle column), and OLR (right column) for the (a) $0.5CO_2$, (b) $1CO_2$, (c) $2CO_2$, and (d) $4CO_2$ simulations. The reference time corresponds to the time when the MJO-filtered anomalies are a minimum over the western Pacific. The gray dashed lines are linear least squares fit estimates of the phase speed and group velocity for the MJO-filtered fields. Circles correspond to the local extremum of each field. Estimate phase speed and group velocities, along with their uncertainties, are shown in the top-left corner of each diagram. Contour interval 1 W m^{-2} for OLR and 0.25 mm for $\langle q' \rangle$.

The region of maximum tropospheric moisture anomalies, shown in Figure 13b, reveals a steady increase in the height of the moisture maximum. Finally, estimates of the rate of change of the phase speed and group velocity estimates from Figure 12 are shown in Figures 13c and 13d. The phase

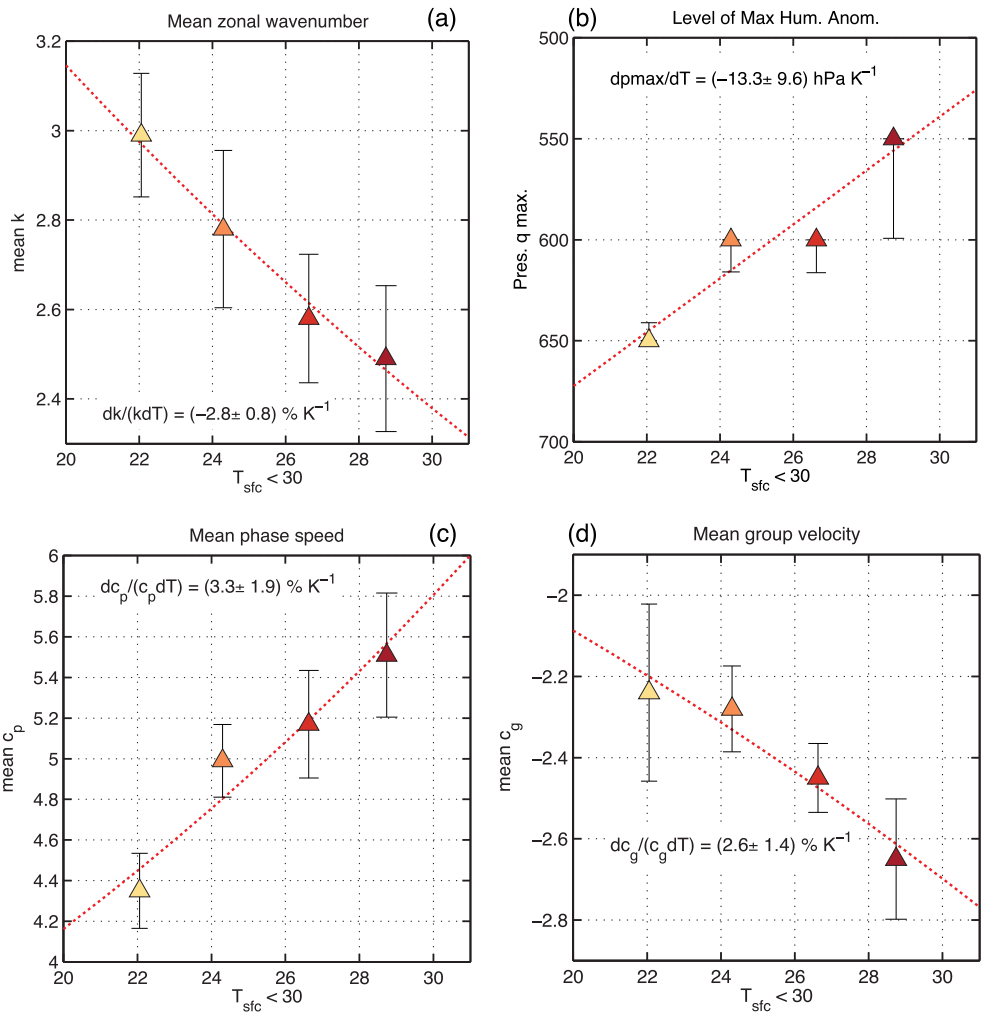

Figure 13. Statistics of the composite MJO for the four GISS simulations. For the mean zonal wave number, a spectral analysis in longitude of the anomalies in Figure 12 is performed, for all days within 25 days of the reference time. The power spectrum is then averaged for all the latitudes and days included and then normalized using the formula $\bar{P}_{xx}(k) = P_{xx}(k)/\Sigma_{k=1}^{N} P_{xx}(k)$. The approximate wave number k is obtained by summing the zonal wave numbers, weighting each one by its normalized power $\bar{P}_{xx}$. The phase speed and group velocities are averaged from the phase speed and group velocities in Figure 12. The dashed line in each plot corresponds to the nonlinear least squares fit of the trend in each variable. Error bars correspond to the spread that arises from varying the zonal wave numbers retained in the MJO filter (varying from retaining zonal wave numbers 1–3 to 1–10) and from subsampling the time series.

speed and group velocity of the MJO increase at similar rates of ∼3.3% K^{-1} and ∼2.6% K^{-1}, respectively. A quantitative analysis of the changes in the MJO's phase speed and group velocity is presented in part II of this study.

6. Concluding Discussion

In this study, we investigated the changes in the MJO as CO_2 concentrations increase. Four 20 year long simulations from the NASA-GISS model with a mixed layer ocean (Q-flux), and a modified convection scheme [*Del Genio et al.*, 2012], with CO_2 concentrations ranging from half to quadruple of preindustrial levels are analyzed. The model exhibits MJO-like variability reminiscent to observations. This study adds to previous studies on how the MJO changes with increasing CO_2 [*Arnold et al.*, 2015; *Chang et al.*, 2015; *Wolding et al.*, 2017, among others].

Results from the four simulations support many previously documented changes in the mean state associated with greenhouse gas induced warming. Column-integrated water vapor concentrations increase

following the Clausius-Clapeyron equation (∼7% K^{-1}), while mean precipitation increases at a fraction of that rate (∼3% K^{-1}) and column relative humidity remains approximately fixed. Furthermore, zonal cross sections reveal increasing relative humidity in the upper-troposphere, increasing static stability and a larger vertical moisture gradient. Moreover, variability over the Indo-Pacific warm pool (60°E–180°E, 15°N/S), defined as the domain-averaged standard deviation, increases at nearly the same rate as the mean state does. However, it is found that moisture and precipitation variability over the MJO's spatial and temporal scales (20–100 day time scale, eastward-propagating zonal wave numbers 1–5) increases at a faster rate of ∼9% K^{-1} and ∼5.6% K^{-1}, consistent with the results of *Arnold et al*. [2013, 2015].

Does the amplification of MJO variability (i.e., power) indicates a destabilization of the wave with warming, or is it a consequence of the overall tropical rain variability change? To address this question, the east-west power ratio, the ratio between spectral power over the MJO band and its westward counterpart, is obtained from each simulation and its relationship with warming is examined. If the amplification is a result of a stronger destabilization of the MJO in a warmer climate, the ratio will show strong positive trend as the MJO variability shows. The east-west power increases only modestly with warming at a rate that is much smaller than that for the MJO variability in both precipitation (∼1.8% K^{-1}) and moisture (∼0.6% K^{-1}), suggesting that it is likely that the increase in MJO variability with warming is mainly associated with changes in tropical rainfall variability.

That the power spectrum of moisture and precipitation increases more quickly at lower frequencies and smaller wave numbers, without preference of direction of propagation indicates that the tropical spectrum of precipitation is becoming more "red." This strengthening in the power over these spectral bands is the result of an increase in the lag-1 spatial and temporal autocorrelation of moisture and precipitation, and might not be due to a destabilization of the MJO. An increase in this correlation would cause the spectrum of moisture and precipitation to shift to lower frequencies and wave numbers, thereby "reddening" the spectrum (see Figure 13 in *Lin et al*. [2006]). We have verified that the lag-1 autocorrelation of column water vapor and precipitation do indeed increase in the GISS model (not shown).

How does a change in the tropical rainfall spectrum affect the MJO? The MJO is often viewed as a large-scale, low-frequency modulation of convection. The modulation of the individual convective events is thought to occur through changes in tropospheric moisture [*Raymond*, 2000; *Holloway and Neelin*, 2009; *Adames*, 2017]. In a warmer climate, with more moisture, individual convective events become more intense, and that would enhance power across scales including that of the MJO band. The moisture residence time scale becomes longer in a warmer climate [*Trenberth*, 1998; *Bosilovich et al*., 2005; *Singh et al*., 2016], therefore its lag-1 correlation increases. This increasing time scale of water vapor in the atmosphere would further contribute to the increase in power of the low-frequency, large-scale modes, even without changing the stability of the MJO. Thus, one should be cautious when linking the amplification of intraseasonal anomalies to changes in MJO maintenance (i.e., destabilization). It is worth mentioning that other models show a more rapid increase in the east-west ratio [*Arnold et al*., 2015; *Carlson and Caballero*, 2016]. It would be interesting to further understand what causes the east-west ratio to increase more rapidly in these models.

Through the use of space-time spectral anomalies and linear regression analysis of OLR over the western Pacific, the changes in the MJO as surface temperatures increase were documented. Results from the spectral analysis reveal a shift towards lower wave numbers (larger scale) and higher frequency (faster propagation) in the MJO, consistent with previous studies [*Arnold et al*., 2013, 2015; *Chang et al*., 2015; *Pritchard and Yang*, 2016]. This change is evident in the precipitation and moisture signal, as well as their coherence squared. Because the climatological-mean lower tropospheric winds were found to change little with increasing CO_2 (Figure 5), we can conclude that the increase in MJO propagation cannot be due to advection of the precipitation anomalies by the mean flow. Instead, it is likely due to increasing horizontal and vertical moisture advection by the MJO-related flow, due to increasing horizontal and vertical moisture gradients, as suggested by *Arnold et al*. [2013, 2015].

Linear regression analysis further reveals that the increase in the MJO phase speed is at a rate of ∼3.3% K^{-1}. Consistent with the study of *Adames and Kim* [2016], a westward group velocity of the MJO was also found in this study, whose amplitude increases with surface temperatures at a rate of ∼2.6% K^{-1}. It is also found that the MJO-related moisture anomalies become deeper as CO_2 concentrations increase, with the peak moisture anomalies occurring ∼13 hPa higher in the troposphere per degree of tropical warming. This deepening of the moisture anomalies may be due to the deepening troposphere that results from warming,

along with changes in the vertical profile of temperature, which affects moisture through the Clausius-Clapeyron equation.

While the results shown in this study give us some insight onto the trends in the structure and propagation of the MJO with climate change, they do not provide sufficient physical and quantitative insights as to why these changes occur in the GISS simulations. Previous studies [*Arnold et al*., 2013; *Maloney and Xie*, 2013; *Wolding et al*., 2017, among others] have suggested that changes in the climatological-mean horizontal and vertical moisture gradients, as well as changes in the dry static stability play a key role in the changing MJO behavior as the climate warms. The high coherence between moisture and precipitation in Figure 8 suggests suggests that we can use a moisture-mode perspective of the MJO to interpret the results found here [*Adames and Kim*, 2016]. Such a quantitative analysis is shown in a companion paper (part II).

Acknowledgments
This work was supported by National Aeronautics and Space Administration grant NNX13AM18G. D. Kim was also supported by the Korea Meteorological Administration Research and Development Program under grant KMIPA 2016–6010 and by the startup grant from the University of Washington. Data used to create the plots in this paper can be downloaded from https://sites.google.com/view/afadames/supplements. Model output from the version of the GISS model used here may be obtained by contacting Daehyun Kim at daehyun@uw.edu. We thank Mike Pritchard, Thorsten Mauritsen and an anonymous reviewer for comments that helped improve the manuscript.

References

Adames, Á. F. (2017), Precipitation budget of the Madden-Julian Oscillation, *J. Atmos. Sci.*, doi:10.1175/JAS-D-16-0242.1.
Adames, Á. F., and J. M. Wallace (2014), Three-dimensional structure and evolution of the MJO and its relation to the mean flow, *J. Atmos. Sci.*, *71*(6), 2007–2026.
Adames, Á. F., and J. M. Wallace (2015), Three-dimensional structure and evolution of the moisture field in the MJO, *J. Atmos. Sci.*, *72*(10), 3733–3754.
Adames, Á. F., and D. Kim (2016), The MJO as a dispersive, convectively coupled moisture wave: Theory and observations, *J. Atmos. Sci.*, *73*(3), 913–941.
Allen, M. R., and W. J. Ingram (2002), Constraints on future changes in climate and the hydrologic cycle, *Nature*, *419*(6903), 224–232.
Arnold, N. P., Z. Kuang, and E. Tziperman (2013), Enhanced MJO-like variability at high SST, *J. Clim.*, *26*(3), 988–1001.
Arnold, N. P., M. Branson, Z. Kuang, D. A. Randall, and E. Tziperman (2015), MJO intensification with warming in the superparameterized CESM, *J. Clim.*, *28*(7), 2706–2724.
Bosilovich, M. G., S. D. Schubert, and G. K. Walker (2005), Global changes of the water cycle intensity, *J. Clim.*, *18*(10), 1591–1608, doi:10.1175/JCLI3357.1.
Caballero, R., and M. Huber (2010), Spontaneous transition to superrotation in warm climates simulated by CAM3, *Geophys. Res. Lett.*, *37*, L11701, doi:10.1029/2010GL043468,.
Carlson, H., and R. Caballero (2016), Enhanced mjo and transition to superrotation in warm climates, *J. Adv. Model. Earth Syst.*, *8*(1), 304–318, doi:10.1002/2015MS000615.
Chang, C.-W. J., W.-L. Tseng, H.-H. Hsu, N. Keenlyside, and B.-J. Tsuang (2015), The Madden-Julian Oscillation in a warmer world, *Geophys. Res. Lett.*, *42*, 6034–6042, doi:10.1002/2015GL065095.
Chikira, M. (2014), Eastward-propagating intraseasonal oscillation represented by Chikira–Sugiyama cumulus parameterization: Part II: Understanding moisture variation under weak temperature gradient balance, *J. Atmos. Sci.*, *71*(2), 615–639.
Chikira, M., and M. Sugiyama (2013), Eastward-propagating intraseasonal oscillation represented by Chikira–Sugiyama cumulus parameterization. part i: Comparison with observation and reanalysis, *J. Atmos. Sci.*, *70*(12), 3920–3939, doi:10.1175/JAS-D-13-034.1.
Chou, C., J. D. Neelin, C.-A. Chen, and J.-Y. Tu (2009), Evaluating the "Rich-Get-Richer" mechanism in tropical precipitation change under global warming, *J. Clim.*, *22*(8), 1982–2005, doi:10.1175/2008JCLI2471.1.
Del Genio, A. D., Y. Chen, D. Kim, and M.-S. Yao (2012), The MJO transition from shallow to deep convection in CloudSat/CALIPSO data and GISS GCM simulations, *J. Clim.*, *25*(11), 3755–3770.
Duchon, C. E. (1979), Lanczos filtering in one and two dimensions, *J. Appl. Meteorol.*, *18*(8), 1016–1022.
Gill, A. E. (1980), Some simple solutions for heat-induced tropical circulation, *Q. J. R. Meteorol. Soc.*, *106*(449), 447–462.
Hayashi, Y. (1981), Space-time spectral analysis and its application to atmospheric waves, *J. Meteorol. Soc. Jpn.*, *60*, 156–171.
Held, I. M., and B. J. Soden (2006), Robust responses of the hydrological cycle to global warming, *J. Clim.*, *19*(21), 5686–5699, doi:10.1175/JCLI3990.1.
Hendon, H. H., and M. C. Wheeler (2008), Some space-time spectral analyses of tropical convection and planetary-scale waves, *J. Atmos. Sci.*, *65*(9), 2936–2948.
Herman, M. J., Z. Fuchs, D. J. Raymond, and P. Bechtold (2016), Convectively coupled Kelvin waves: From linear theory to global models, *J. Atmos. Sci.*, *73*(1), 407–428, doi:10.1175/JAS-D-15-0153.1.
Holloway, C. E., and J. D. Neelin (2009), Moisture vertical structure, column water vapor, and tropical deep convection, *J. Atmos. Sci.*, *66*(6), 1665–1683.
Jones, C., and L. Carvalho (2011), Will global warming modify the activity of the Madden–Julian Oscillation?, *Q. J. R. Meteorol. Soc.*, *137*(655), 544–552.
Kim, D., et al. (2009), Application of MJO simulation diagnostics to climate models, *J. Clim.*, *22*(23), 6413–6436.
Kim, D., A. H. Sobel, A. D. D. Genio, Y. Chen, S. J. Camargo, M.-S. Yao, M. Kelley, and L. Nazarenko (2012), Tropical subseasonal variability simulated in the Nasa Giss general circulation model, *J. Clim.*, *25*, 4641–4659.
Lau, W. K.-M., and D. E. Waliser (2011), *Intraseasonal Variability in the Atmosphere-Ocean Climate System*, Springer, Berlin.
Lin, J.-L., et al. (2006), Tropical intraseasonal variability in 14 IPCC AR4 climate models: Part I: Convective signals, *J. Clim.*, *19*(12), 2665–2690.
Liu, P., T. Li, B. Wang, M. Zhang, J.-j. Luo, Y. Masumoto, X. Wang, and E. Roeckner (2013), MJO change with A1B global warming estimated by the 40-km ECHAM5, *Clim. Dyn.*, *41*(3–4), 1009–1023.
Madden, R., and P. Julian (1971), Detection of a 40–50 day oscillation in the zonal wind in the tropical Pacific, *J. Atmos. Sci.*, *28*, 702–708, doi:10.1175/1520-0469(1971)028 < 0702DOADOI>2.0.CO;2.
Madden, R., and P. Julian (1972), Description of global scale circulation cells in the tropics with a 40–50 day period, *J. Atmos. Sci.*, *29*, 1109–1123, doi:10.1175/1520-0469(1972)029 < 1109:DOGSCC>2.0.CO;2.
Maloney, E. D., and S.-P. Xie (2013), Sensitivity of tropical intraseasonal variability to the pattern of climate warming, *J. Adv. Model. Earth Syst.*, *5*(1), 32–47.

Masunaga, H. (2007), Seasonality and regionality of the Madden-Julian oscillation, Kelvin wave and equatorial Rossby wave, *J. Atmos. Sci.*, *64*, 4400–4416, doi:10.1175/2007JAS2179.1.
Matsuno, T. (1966), Quasi-geostrophic motions in the equatorial area, *J. Meteorol. Soc. Jpn.*, *44*, 25–43.
O'Gorman, P. A., R. P. Allan, M. P. Byrne, and M. Previdi (2012), Energetic constraints on precipitation under climate change, *Surv. Geophys.*, *33*(3), 585–608, doi:10.1007/s10712-011-9159-6.
Pendergrass, A. G., and D. L. Hartmann (2014), The atmospheric energy constraint on global-mean precipitation change, *J. Clim.*, *27*(2), 757–768, doi:10.1175/JCLI-D-13-00163.1.
Pritchard, M. S., and D. Yang (2016), Response of the superparameterized Madden-Julian Oscillation to extreme climate and basic state variation challenges a moisture mode view, *J. Clim.*, *29*(7), 4995–5008, doi:10.1175/JCLI-D-15-0790.1.
Raymond, D. J. (2000), Thermodynamic control of tropical rainfall, *Q. J. R. Meteorol. Soc.*, *126*(564), 889–898, doi:10.1002/qj.49712656406.
Raymond, D. J., and Ž. Fuchs (2009), Moisture modes and the Madden–Julian Oscillation, *J. Clim.*, *22*(11), 3031–3046.
Schmidt, G., et al. (2014), Tropical subseasonal variability simulated in the NASA GISS general circulation model, *J. Adv. Model. Earth Syst.*, *6*, 141–184, doi:10.1002/2013MS000265.
Seager, R., N. Naik, and G. A. Vecchi (2010), Thermodynamic and dynamic mechanisms for large-scale changes in the hydrological cycle in response to global warming, *J. Clim.*, *23*(17), 4651–4668, doi:10.1175/2010JCLI3655.1.
Singh, H. K. A., C. M. Bitz, A. Donohoe, J. Nusbaumer, and D. C. Noone (2016), A mathematical framework for analysis of water tracers. Part ii: Understanding large-scale perturbations in the hydrological cycle due to CO_2 doubling, *J. Clim.*, *29*(18), 6765–6782, doi:10.1175/JCLI-D-16-0293.1.
Slingo, J. M., D. P. Rowell, K. R. Sperber, and F. Nortley (1999), On the predictability of the interannual behaviour of the Madden-Julian oscillation and its relationship with el ni?o, *Q. J. R. Meteorol. Soc.*, *125*(554), 583–609, doi:10.1002/qj.49712555411.
Sobel, A., and E. Maloney (2012), An idealized semi-empirical framework for modeling the Madden-Julian oscillation, *J. Atmos. Sci.*, *69*(5), 1691–1705.
Sobel, A., and E. Maloney (2013), Moisture modes and the eastward propagation of the MJO, *J. Atmos. Sci.*, *70*(1), 187–192.
Sobel, A. H., and C. S. Bretherton (2003), Large-scale waves interacting with deep convection in idealized mesoscale model simulations, *Tellus, Ser. A*, *55*(1), 45–60.
Song, E.-J., and K.-H. Seo (2016), Past- and present-day Madden-Julian oscillation in CNRM-CM5, *Geophys. Res. Lett.*, *43*, 4042–4048, doi:10.1002/2016GL068771.
Sperber, K. R., and D. Kim (2012), Simplified metrics for the identification of the Madden-Julian oscillation in models, *Atmos. Sci. Lett.*, *13*(3), 187–193, doi:10.1002/asl.378.
Subramanian, A., M. Jochum, A. J. Miller, R. Neale, H. Seo, D. Waliser, and R. Murtugudde (2014), The MJO and global warming: A study in CCSM4, *Clim. Dyn.*, *42*(7–8), 2019–2031.
Taylor, K. E., R. J. Stouffer, and. G. A. Meehl (2012), An overview of CMIP5 and the experiment design, *Bull. Am. Meteorol. Soc.*, *93*, 485–498.
Trenberth, K. E. (1998), Atmospheric moisture residence times and cycling: Implications for rainfall rates and climate change, *Clim. Change*, *39*(4), 667–694.
Waliser, D., et al. (2009), MJO simulation diagnostics, *J. Clim.*, *22*, 3006–3030, doi:10.1175/2008JCLI2731.1.
Wheeler, M., and G. N. Kiladis (1999), Convectively coupled equatorial waves: Analysis of clouds and temperature in the wavenumber-frequency domain, *J. Atmos. Sci.*, *56*, 374–399, doi:10.1175/1520-0469(1999)056 < 0374:CCEWAO > 2.0.CO;2.
Wolding, B. O., and E. D. Maloney (2015), Objective diagnostics and the Madden-Julian Oscillation. Part II: Application to moist static energy and moisture budgets, *J. Clim.*, *28*(19), 7786–7808, doi:10.1175/JCLI-D-14-00689.1.
Wolding, B. O., E. D. Maloney, S. Henderson, and M. Branson (2017), Climate change and the Madden-Julian oscillation: A vertically resolved weak temperature gradient analysis, *J. Adv. Model. Earth Syst.*, *9*, 307–331, doi:10.1002/2016MS000843.
Yanai, M., and M. Murakami (1970), Spectrum analysis of symmetric and anti-symmetric equatorial waves, *J. Meteorol. Soc. Jpn.*, *48*, 331–347, doi:10.1175/1520-0469(2000)057 < 0613:LSDFAW > 2.0.CO;2.
Yao, M.-S., and Y. Cheng (2012), Cloud simulations in response to turbulence parameterizations in the GISS model E GCM, *J. Clim.*, *25*, 4963–4974.
Yasunaga, K., and B. Mapes (2012), Differences between more divergent and more rotational types of convectively coupled equatorial waves. Part I: Space-time spectral analyses, *J. Atmos. Sci.*, *69*(1), 3–16.
Zhang, C. (2005), Madden-Julian Oscillation, *Rev. Geophys.*, *43*, RG2003, doi:10.1029/2004RG000158.
Zhang, C. (2013), Madden-Julian Oscillation: Bridging weather and climate, *Bull. Am. Meteorol. Soc.*, *94*(12), 1849–1870.